Mineralium Deposita (2019) 54:459–472
https://doi.org/10.1007/s00126-018-0816-2

ARTICLE

Mineralogy and titanite geochronology of the Caojiaba W deposit, Xiangzhong metallogenic province, southern China: implications for a distal reduced skarn W formation

Guiqing Xie[1] · Jingwen Mao[1] · Leon Bagas[1,2] · Bin Fu[3] · Zhiyuan Zhang[1]

Received: 25 September 2017 / Accepted: 31 May 2018 / Published online: 6 July 2018

Abstract

The Caojiaba tungsten deposit (19.03 Mt@ 0.37 wt% WO_3) is hosted by skarn along the contact between clastic and carbonate rocks in the Xiangzhong Metallogenic Province of southern China. The deposit is characterized by an early prograde skarn containing low andraditic garnet ($Ad_{0.7–21.9}$) and hedenbergitic pyroxene ($Hd_{52.9–77.3}$) overprinted by a retrograde biotite–chlorite assemblage and then by quartz–scheelite veins, similar to well-studied reduced tungsten skarns worldwide. Scheelite has low MoO_3 (0.01–0.16 wt%), and ore commonly contains up to 1.5 ppm Au and up to 0.33 wt% Sb. Sensitive high-resolution ion microprobe (SHRIMP) U–Pb analyses of hydrothermal titanite coexisting with scheelite in three skarn ore samples provide ages between 206 ± 5 Ma and 196 ± 3 Ma (2σ). Our new ages demonstrate that the tungsten mineralization took place at Caojiaba between 206 and 196 Ma, overlapping the 228–201 Ma emplacement age of granitic rocks in the Xiangzhong Metallogenic Province. Mineralogical and geochronological evidence collectively indicates that Caojiaba is a distal reduced W skarn deposit. The 226–196 Ma granite-related W mineralization recognized throughout the province has a possible link with the widespread Sb–Au mineralization in the region.

Keywords Caojiaba · Distal reduced skarn · Tungsten deposit · Titanite dating · South China

Introduction

Tungsten skarn deposits supply over 70% of the global W resource (Kwak 1987), and they are commonly associated with coarse-grained, equigranular plutons that are surrounded by high-temperature metamorphic aureoles (Meinert et al. 2005). However, some tungsten-bearing skarns are stratiform and continuous for hundreds of metres along lithological contacts (Einaudi et al. 1981). There is uncertainty regarding the genesis of such "stratiform" or "stratabound" tungsten deposits that are not near exposed granitic intrusions but nevertheless are associated with skarn-type mineralogy. These deposits are interpreted as being either granite-related or syngenetic in origin (Raith and Stein 2000). Kwak (1987) documented the presence of ambiguous Precambrian tungsten-bearing skarn deposits located more than 5 km from known igneous contacts. Precise dating of such deposits is particularly important for understanding the origin of the "stratabound" tungsten deposit.

Southern China hosts giant Mesozoic granite-related W–Sn deposits to the east, and low-temperature Sb–Au deposits to the west (Mao et al. 2013). The Xiangzhong Metallogenic Province (XZMP) in the west (Fig. 1), which contains numerous Sb–Au deposits, is one of the most important low-temperature (< 250 °C) metallogenic domains in southern China, and it contains > 50% of the Earth's known Sb resources (Hu et al. 2017a). In addition to low-temperature Sb–Au deposits, skarn, and quartz

Editorial handling: R. L. Romer

Electronic supplementary material The online version of this article (https://doi.org/10.1007/s00126-018-0816-2) contains supplementary material, which is available to authorized users.

✉ Guiqing Xie
xieguiqing@cags.ac.cn

[1] Key Laboratory of Metallogeny and Mineral Assessment, Ministry of Land and Resources of the People's Republic of China (MLR), Institute of Mineral Resources, Chinese Academy of Geological Sciences, No.26 Baiwanzhuang Road, Beijing 100037, People's Republic of China

[2] Centre for Exploration Targeting, The University of Western Australia, Crawley, WA 6009, Australia

[3] Research School of Earth Sciences, The Australian National University, ACT, Canberra 2601, Australia

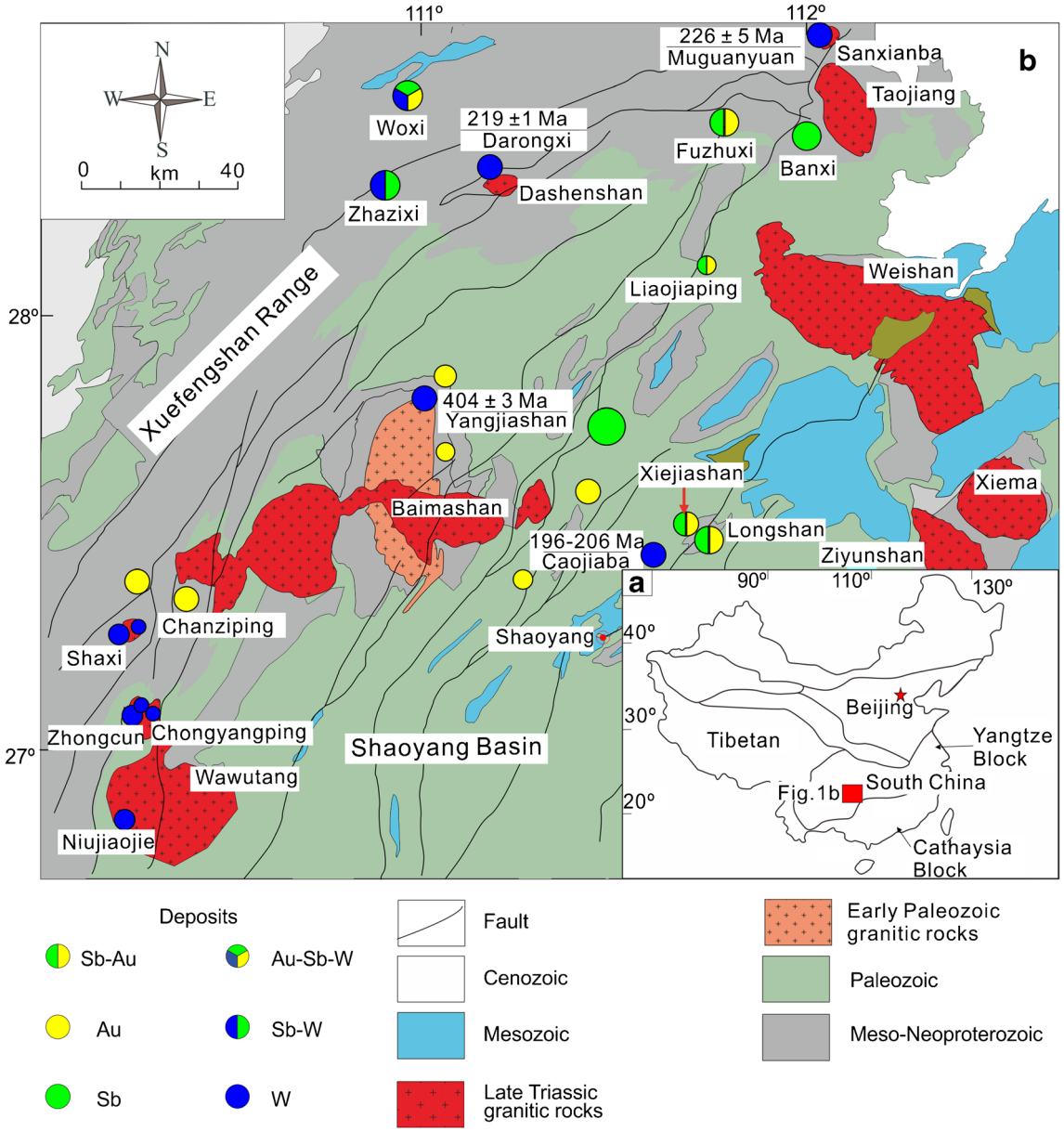

Fig. 1 Regional geological map of XZMP in southern China, showing the distribution, and timing of granitic intrusions and important Sb, Au, and W deposits (modified after Geological Map of the Hunan Province). Figure 1a shows tectonic framework of China including the location of XZMP

vein- and stockwork-hosted W deposits are present in XZMP (Fig. 1b). The Caojiaba skarn deposit is the largest among these tungsten deposits. It is hosted at the contact between Devonian clastic and carbonate rocks, and outcropping granitic rocks are not seen near deposit (Qian and Jiang 1983).

The genesis of the Caojiaba tungsten deposit remains uncertain, particularly as the precise age of the mineralization and a possible genetic link to magmatism are not clear. Furthermore, an understanding of the relationship between W and Sb–Au deposits is lacking in XZMP.

This paper presents new geological, mineralogical, and titanite SHRIMP U–Pb data for the Caojiaba tungsten deposit. These data are used to better constrain the processes responsible for the genesis of the deposit, and further evaluate the possible relationship between W and Sb–Au deposits in XZMP of southern China.

Geological setting

Southern China is subdivided into the Yangtze Block in the northwest and Cathaysia Block in the southeast (Fig. 1a). The XZMP is located in the eastern part of the Yangtze Block, and includes the Xuefengshan Range in the west and the Shaoyang Basin in the east (Fig. 1b). The Mesoproterozoic Lengjiaxi Group and the Neoproterozoic Banxi Group are present in this

region, which regionally metamorphosed to be sub-greenschist facies between 1000 Ma and 800 Ma (HNBGMR 1988). The Neoproterozoic sedimentary rock sequences consist of conglomerate, sandstone, siltstone, shale, and chert intercalated with minor carbonate rocks, and they are exposed in a domical structure in the central part of the Shaoyang Basin. Phanerozoic units include shallow marine Cambrian to Ordovician carbonate–siliciclastic successions, Silurian shale and sandstone, Devonian to Permian limestone and subordinate clastic rocks containing coal seams, and an Early Jurassic to Cretaceous terrestrial sequence (Tang et al. 2014).

Sedimentary units of XZMP are intruded by widespread Late Triassic and subordinate early Paleozoic granitic rocks (Fig. 1b), which probably formed by partial melting of the Proterozoic metasedimentary rocks (Chu et al. 2012a; Fu et al. 2015). Zircon SHRIMP and LA–ICPMS U–Pb ages demonstrate that the Late Triassic granitic plutons were emplaced over a lengthy period between 228 and 201 Ma along the margin of the Shaoyang Basin (Fig. 1b; ESM Table 1). More than 170 Sb–Au deposits have been discovered in XZMP, and they are hosted in Proterozoic to Cambrian clastic rocks, Devonian to Carboniferous carbonate rocks, and felsic dykes (Hu and Zhou 2012; Peng and Frei 2004).

Two contrasting types of tungsten deposits have also been recognized in XZMP. Firstly, scheelite is a common ore mineral in most Sb–Au deposits hosted by the Proterozoic metamorphosed clastic rocks (Fig. 1b). Examples include the Zhazixi Sb–W and Woxi Au–Sb–W deposits (Zhu and Peng 2015; Zhao et al. 2017) (Fig. 1b). Secondly, scheelite in quartz veins and veinlet at the Muguanyuan, Yangjiashan, Shaxi, Zhongcun and Niujiaojie tungsten deposits, as well as in skarn assemblages at the Caojiaba and Darongxi tungsten deposits (Fig. 1b). These scheelite-bearing deposits have all been recognized as being granite-related, including Devonian quartz–veins at Yangjiashan (Xie et al. 2018); Late Triassic disseminated and veinlet-hosted ore at Muguanyuan, quartz vein-hosted mineralization at Shaxi, Zhongcun, and Niujiaojie, and the Darongxi and Caojiaba skarn deposits (Zhang 2013; Zhang et al. 2014, 2016; Su et al. 2016; Tang et al. 2016).

Deposit geology

The Caojiaba scheelite deposit was discovered in the late 1970s, and evaluated during 2010 to 2014 by the No. 407 Geological Team of the Bureau of Geology and Mineral Exploration and Development of Hunan Province. The deposit has a resource of 19.03 Mt.@ 0.37 wt% WO_3 (HNBGMR 2015). The tungsten mineralization in the northeastern part of the deposit contains 0.1 to 1.5 ppm Au and 0.10 to 0.33 wt% Sb, which are recovered as by-products (Fig. 2a).

The region around Caojiaba is underlain by rocks of the Middle Devonian Tiaomajian and Qiziqiao Formations, and Late Devonian Shetianqiao Formation (Fig. 2a). The Tiaomajian Formation comprises sandstone, siltstone, and silty mudstone. The Qiziqiao and Shetianqiao Formations consist of limestone and mudstone. Twelve orebodies are hosted along the contact between the Tiaomajian clastic rocks and Qiziqiao carbonate rocks (Figs. 2b and 3). Orebodies in the Tiaomajian and Qiziqiao Formations account for 52 and 48% of the total reserve, respectively (Qian and Jiang 1983). The No. VII orebody (Fig. 3) is the largest orebody, occurring as steeply NW-dipping (45°–55°). It is 1060 m long, 3 to 8 m wide, and continues for 660 m down-dip, and has an average ore grade of 0.38 wt% WO_3.

Rocks of the Tiaomajian and Qiziqiao formations have been subjected to intense hydrothermal alteration, resulting in the formation of a wide variety of skarn and other alteration assemblages (Figs. 4 and 5). Our detailed drill-hole core logging shows that all orebodies were exclusively located within skarn (Fig. 2b). The garnet + pyroxene skarns have overprinted the limestone, mudstone, and siltstone (Figs. 4a–c, e and 5a–b). The contact between the skarn and country rocks is sharp, and the presence of marble has been locally observed (Fig. 4a). Retrograde alteration assemblages include epidote, chlorite, and biotite replacing garnet and pyroxene (Figs. 4d and 5c–e). Mineralization consists of scheelite and pyrrhotite, with subordinate chalcopyrite, pyrite, sphalerite, bismuthinite, wolframite, and stibnite (Figs. 4 and 5). Disseminated scheelite occurs as interstitial grains among the pyroxene and garnet (Figs. 4a–e and 5a–b) and coexists with epidote, biotite, and chlorite replacing garnet (Fig. 5c–e). Quartz–scheelite veins cut all skarn and siltstone (Fig. 4a–b, e–g). Cathodoluminescence (CL) images reveals the presence of oscillatory zoning in coarse-grained scheelite (Fig. 5j). Stibnite coexists with calcite and quartz in the scheelite–sulfide veins at Caojiaba (Fig. 5k). Coarse-grained scheelite coexisting with stibnite veins (Figs. 4j and 5l) are also present in the nearby Xiejiashan Sb–Au(W) deposit (Fig. 1b). Three stages of mineralization have been recognized based on cross-cutting relationships and mineral assemblages (Fig. 6): an early prograde skarn stage (I), a middle retrograde skarn stage (II), and a late quartz–scheelite–sulfide stage (III).

Sampling and methods

More than 200 samples were collected from drill-holes, and three mineralized skarn samples have been investigated in detail in this study. High-grade W skarn ores (CJB 53, CJB 64 and CJB 67) with 1.1 wt%, 1.2 wt%, and 3.7 wt% WO_3, were collected from a depth of 264 m in DDH ZK 801, 557 m in DDH ZK 802, and 659 m in DDH ZK 803 (Fig. 2b), respectively. Titanite grains in the skarn samples were too fine-grained to separate enough material for U–Pb dating using conventional heavy liquid and magnetic techniques. Standard petrographic thin sections were

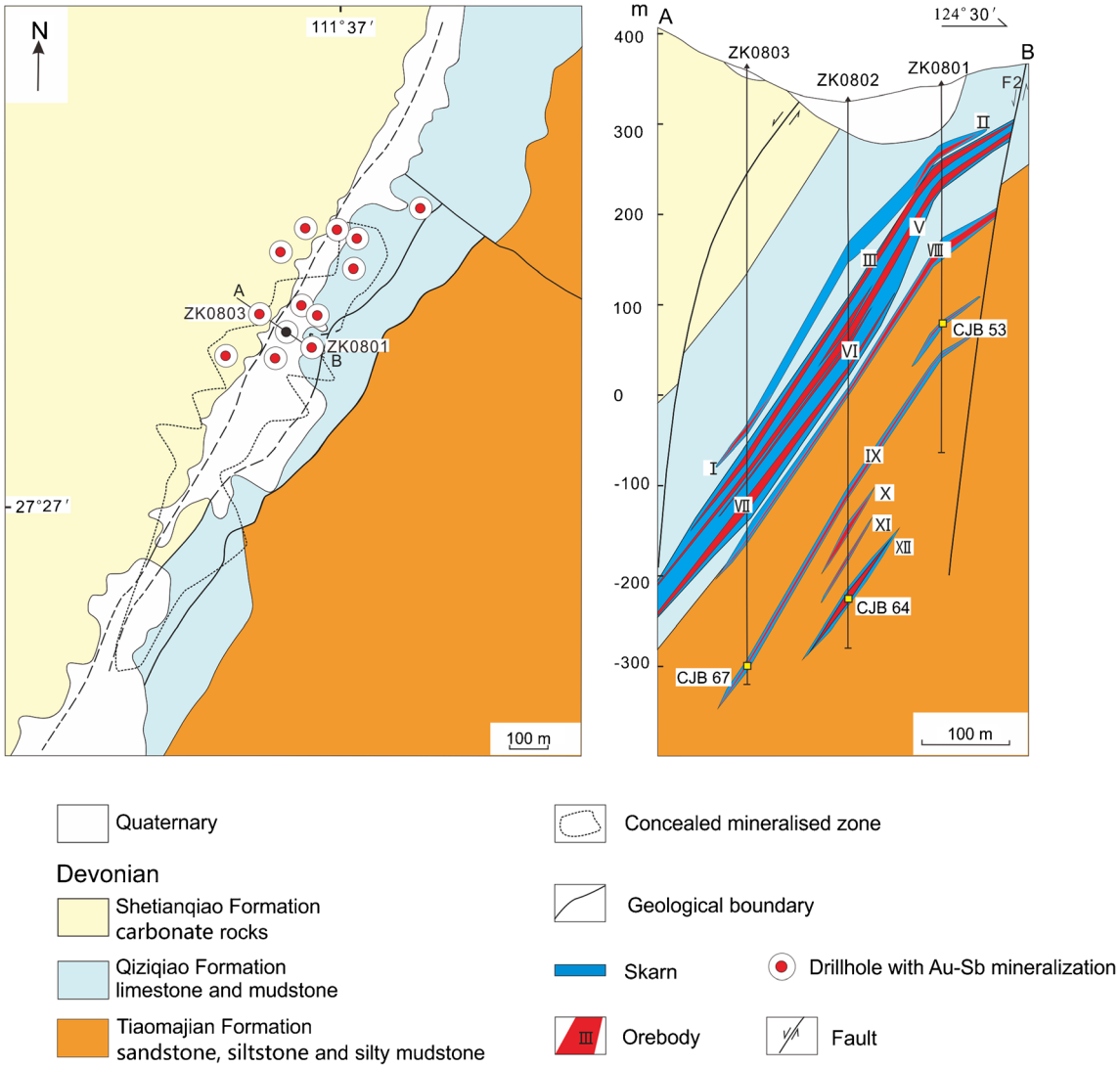

Fig. 2 Simplified geological (**a**) and cross-section (**b**) maps of the Caojiaba tungsten deposit (modified after maps by the No. 407 Geological Team, Bureau of Geology and Mineral Exploration and Development of the Hunan Province)

prepared from three samples for optical microscopy to identify the mineral paragenetic relationships.

The chemical compositions of garnet, pyroxene, scheelite, and titanite grains were determined using a JOELJXA–823 V Electron Probe Microa Analyzer (EPMA) operated with an accelerating voltage of 15 kV, a beam current of 20 nA, and a beam diameter of 5 μm at the MLR Key Laboratory of Metallogeny and Mineral Assessment, Institute of Mineral Resources, Chinese Academy of Geological Sciences. The analyses were calibrated using jadeite (Si, Na, and Al), forsterite (Mg), orthoclase (K), apatite (P), wollastonite (Ca), rutile (Ti), and synthetic oxide (Cr, Mn, Fe, Ni) standards.

Based on petrographic features and EPMA results, 12 chips including titanite grains, were extracted from thin sections using a diamond band saw. The chips and the BLR 1 titanite standard (Aleinikoff et al. 2007) were mounted in epoxy. Mount Z6536 was then gold-coated and examined using the scanning electron microscope with JEOL JSM–6610A at the Research School of Earth Sciences (RSES), Australian National University, Canberra. The microscope was equipped with a Robinson CL detector, and the back-scattered electron (BSE) images were used to examine the shape and internal textures of the titanite studied (Fig. 7).

Uranium–Th–Pb measurements on titanite were made using the SHRIMP II instrument in RSES using a focused, ~4.5 nA (O_2^-) primary beam. Counts were acquired on both the sample and BLR 1 titanite standard with a single-collector mode, and each analysis involved seven scans through the masses on monovalent species $^{200}(CaTi_2O_4)$, ^{204}Pb, ^{206}Pb, ^{207}Pb, ^{208}Pb, ^{238}U, $^{232}Th^{16}O$, and $^{238}U^{16}O$. Given the small size of these titanite grains studied, U–Th–Pb analyses were run initially using 15 μm spots, and then duplicate analyses of sample CJB 67 were run using 30 μm spots. The 15 μm spots pits were polished out before duplicate analyses. The analyzed pits were inspected used

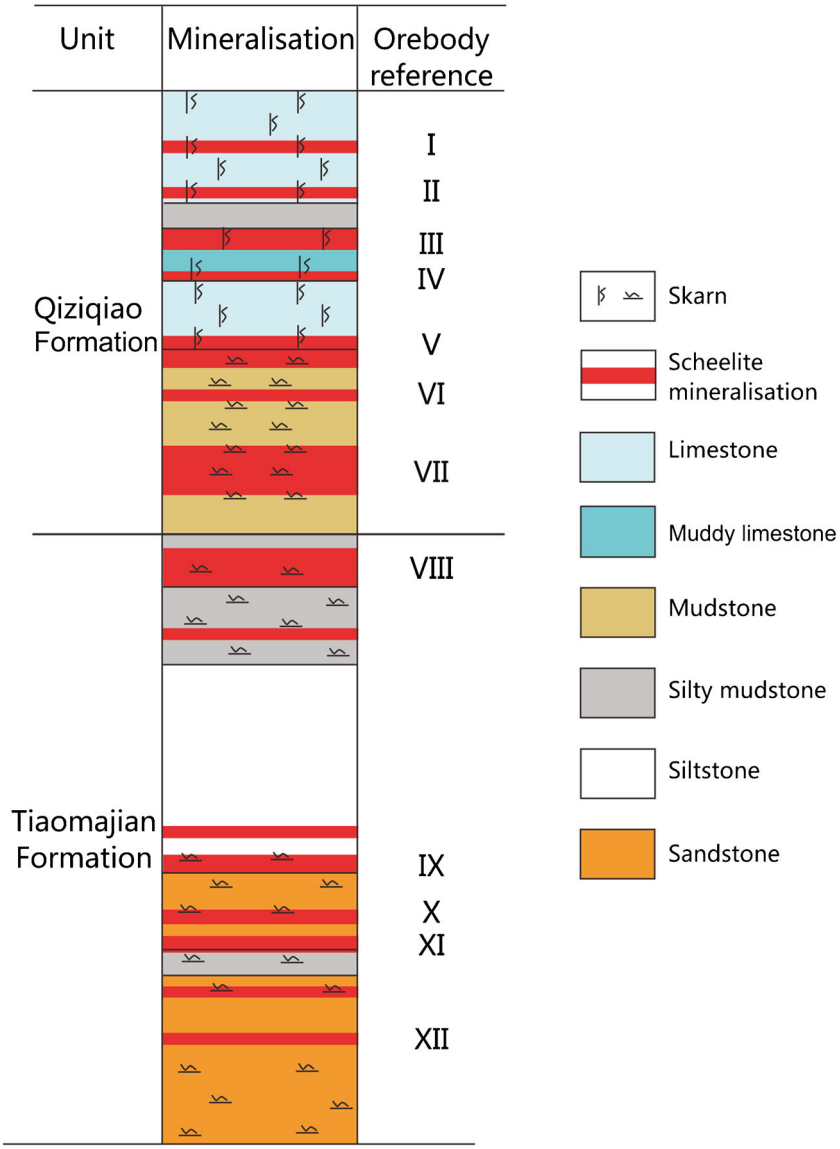

Fig. 3 Stratigraphic succession of sedimentary rocks for the Caojiaba tungsten deposit showing the distribution of orebodies (modified after maps by the No. 407 Geological Team, Bureau of Geology and Mineral Exploration and Development of the Hunan Province)

the SEM, and the data for several spots were discarded because of significant overlap with inclusions and along grain margins. Data were reduced and isotope ratios calculated using the SQUID software and ISOPLOT 4.15 (Ludwig 2012).

Results

Mineral chemistry

The analytical data collected from garnet, pyroxene, titanite, and scheelite from the Caojiaba deposit are given in ESM Table 2. The compositional variations of garnet and pyroxene are plotted in a ternary diagram for comparison with other well-studied reduced and oxidized skarn deposits worldwide (Fig. 8). The Caojiaba skarn is characterized by grossular ($Ad_{0.7–21.9}Gr_{66.2–91.0}$) and hedenenbergite ($Hd_{52.9–77.3}Di_{21.0–44.4}$) (ESM Table 2; Fig. 8). Titanite exhibits relatively uniform SiO_2 (29.84–31.46%) and CaO (27.88–29.04 wt%), low TiO_2 (27.76–36.46 wt%), high Al_2O_3 + FeOT (3.11–7.78 wt%) and F (0.68–2.79 wt%) (ESM Table 2; Fig. 9). Scheelite has relatively uniform WO_3 (78.91–80.63 wt%) and CaO (19.77–20.63 wt%) compositions, which are close to the pure scheelite compositions of 19.5 wt% CaO and 80.5 wt% WO_3. Relatively low concentrations of MoO_3 are present in the early disseminated scheelite in the skarns (0.09–0.16 wt%), and in the late quartz vein–hosted scheelite (0.01–0.09 wt%) (ESM Table 2).

U–Pb titanite dating

The U–Th–Pb isotopic results for titanite grains analyzed in this study are summarized in ESM Table 3. The titanite grains analyzed from three mineralized skarn samples coexist with

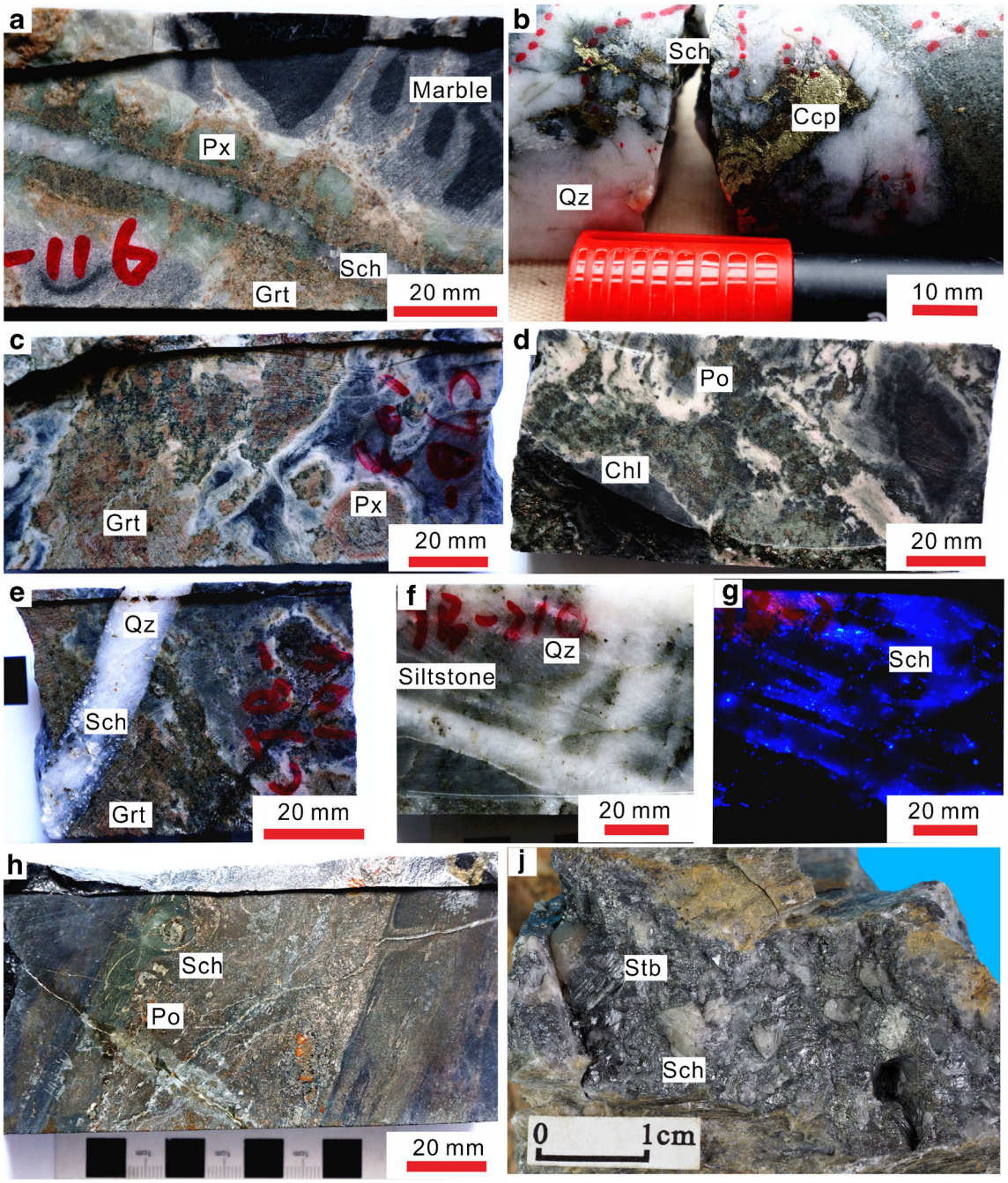

Fig. 4 Tungsten ore specimens showing the mineral assemblages of the Caojiaba tungsten deposit. **a** Quartz–scheelite veinlet with minor marble cutting garnet–pyroxene skarn with disseminated scheelite; **b** coarse-grained scheelite coexisting with chalcopyrite in the quartz vein; **c** pyroxene–garnet skarn overprinting sandstone with disseminated scheelite; **d** retrograde chlorite associated with pyrrhotite and minor scheelite; **e** coarse-grained scheelite quartz veinlet cutting garnet skarn in sandstone; **f** quartz–scheelite veinlet overprinting siltstone; **g** quartz–scheelite veinlet under ultraviolet light showing scheelite with blue luminescence; **h** pyrrhotite coexisting with scheelite veins; **j** coarse-grained scheelite coexisting with stibnite veins at Xiejiashan. *Ccp* chalcopyrite, *Chl* chlorite. *Grt* garnet, *Po* pyrrhotite, *Px* pyroxene, *Qz* quartz, *Sch* scheelite, *Stb* sbitine.

chlorite, biotite, and scheelite (Fig. 7a–c), indicating that titanite from these samples formed during the retrograde skarn alteration stage. The titanite grains are euhedral to subhedral in shape, 30–180 μm long and 20–80 μm wide, and are commonly characterized by irregular and patchy zoning as revealed by BSE imaging (Fig. 7d–f).

The analyzed titanite grains have low U contents or a high percentage of common $^{206}Pb_c$ up to 91.6 wt% (ESM Table 3),

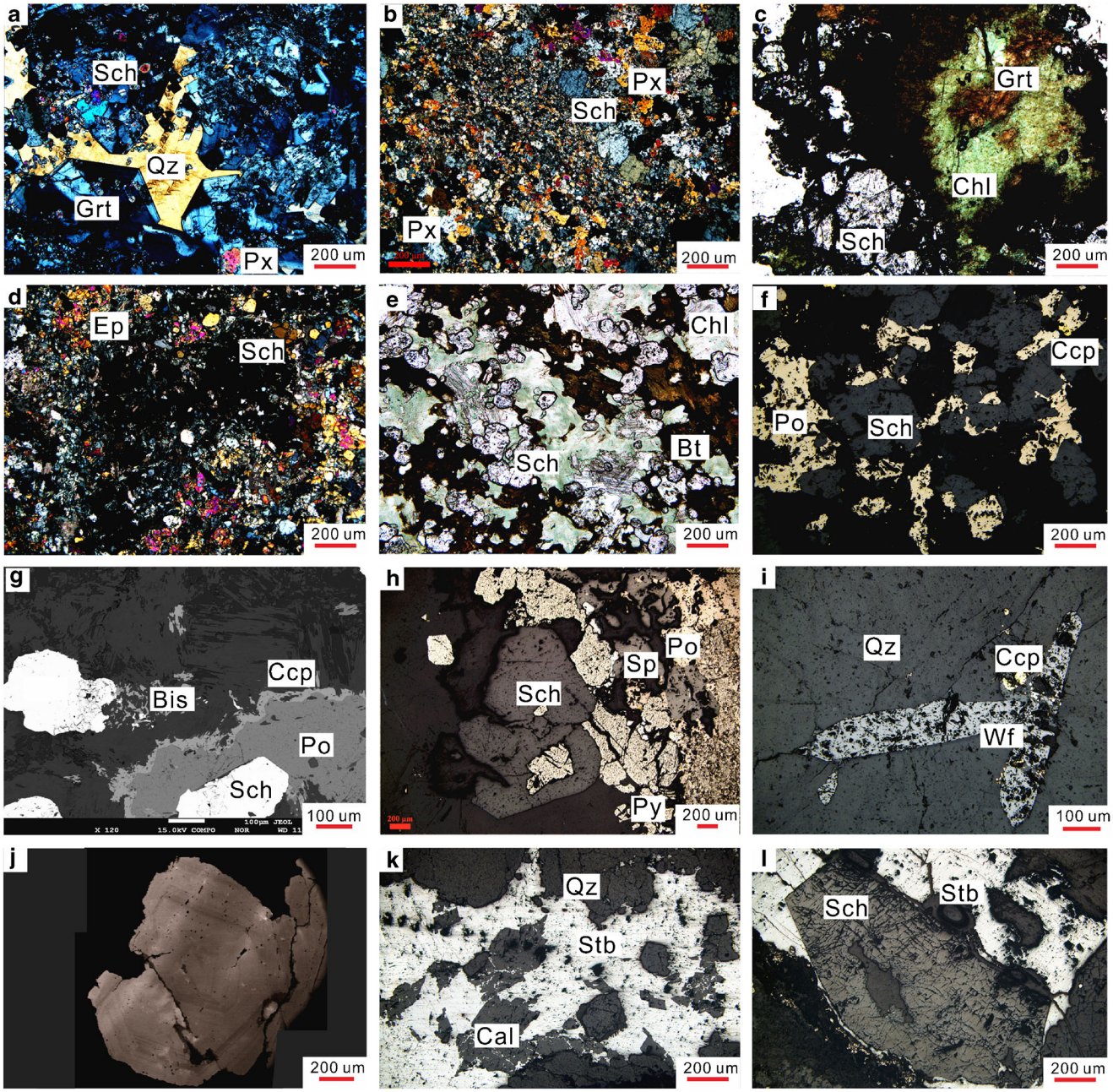

Fig. 5 Photomicrographs showing the mineral assemblages of the Caojiaba tungsten deposit. **a** pyroxene–garnet skarn with quartz and minor disseminated scheelite; **b** pyroxene skarn with minor disseminated scheelite; **c** chlorite replacing garnet coexisting with scheelite; **d** retrograde epidote skarn with disseminated scheelite; **e** retrograde biotite and chlorite coexisting with scheelite; **f** scheelite coexisting with pyrrhotite and chalcopyrite; **g** scheelite coexisting with pyrrhotite, chalcopyrite, and minor bismuthinite; **h** scheelite coexisting with pyrite, sphalerite, and pyrrhotite. **i** quartz–wolframite veinlet with chalcopyrite; **j** CL image of coarse-grained scheelite in the quartz vein; **k** stibnite coexisting with calcite and quartz in the scheelite–sulfide vein; **l** coarse-grained scheelite coexisting with stibnite at Xiejiashan. *Bis* bismuthinite, *Bt* biotite, *Ccp* chalcopyrite, *Chl* chlorite, *Ep* epidote, *Grt* garnet, *Po* pyrrhotite, *Px* pyroxene, *Py* pyrite, *Qz* quartz, *Sp* sphalerite, *Sch* scheelite, *Stb* sbitine, *Wf* wolframite.

such that use of the Stacey and Kramers (1975) model for correcting Pb isotope data is not applicable. This is overcome by the procedure outlined by Aleinikoff et al. (2002), which involves plotting uncorrected isotope data on a Tera–Wasserburg total Pb diagram ($^{238}U/^{206}Pb$–$^{207}Pb/^{206}Pb$; Fig. 10), and with a 3D linear regression applied to the analyses, yielding a lower intercept representing the approximate titanite age. This method is useful when the initial Pb

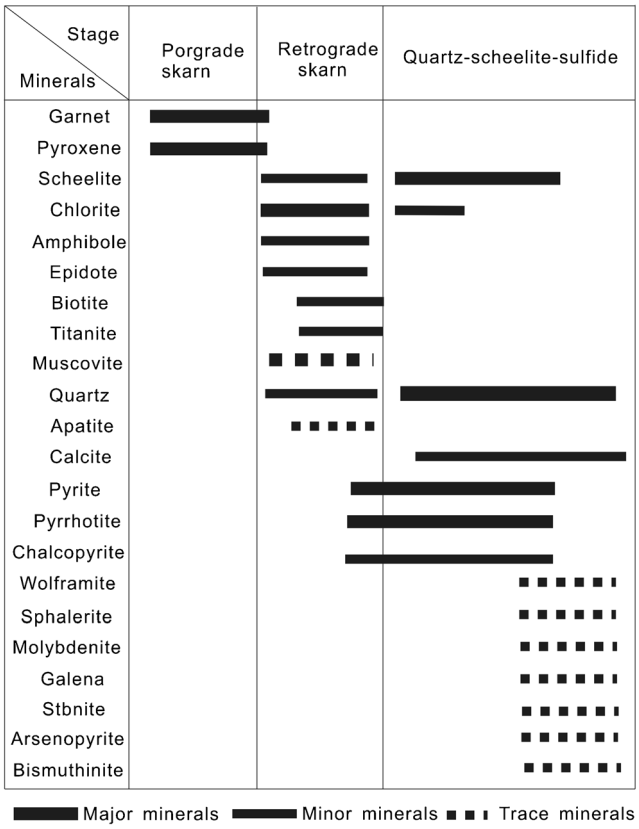

Fig. 6 Paragenesis of the mineral assemblages showing the mineralized sequence of the Caojiaba tungsten deposit

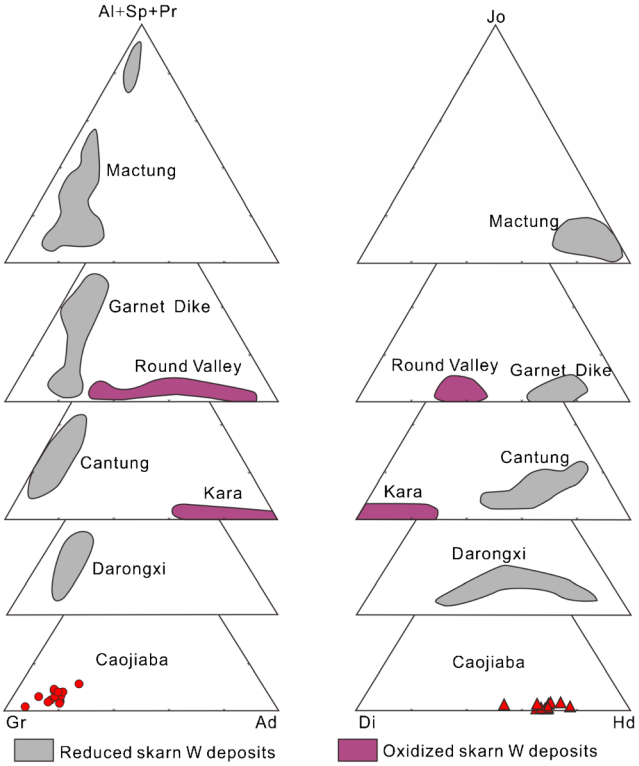

Fig. 8 Ternary diagrams showing compositional variation of garnet (**a**) and pyroxene (**b**) from the Caojiaba tungsten deposit compared with garnet and pyroxene from reduced W skarn deposits at Mactung, Great Dike, and Cantung, and oxidized W skarn deposits at Round Valley and Kara (Einaudi et al. 1981; Zaw and Singoyi 2000), as well as the Darongxi tungsten deposit (Zhang 2013)

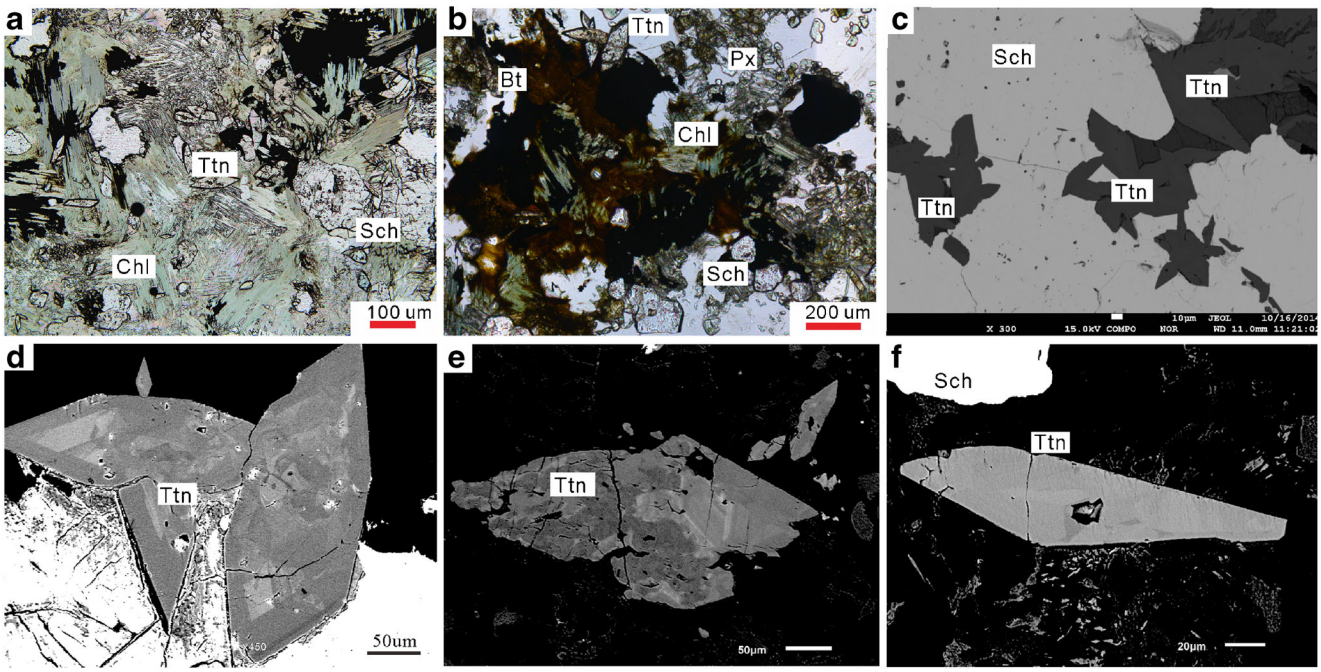

Fig. 7 Photomicrographs of titanite of the Caojiaba tungsten deposit. **a** Euhedral titanite coexisting with chlorite and scheelite; **b** euhedral titanite coexisting with biotite, scheelite and chlorite; **c** BSE image of euhedral titanite enclosed in scheelite; **d**–**f** BSE image showing internal textures of titianite. *Ttn* titanite, *Sch* scheelite, *Chl* chlorite, *Px* pyroxene, *Bt* biotite

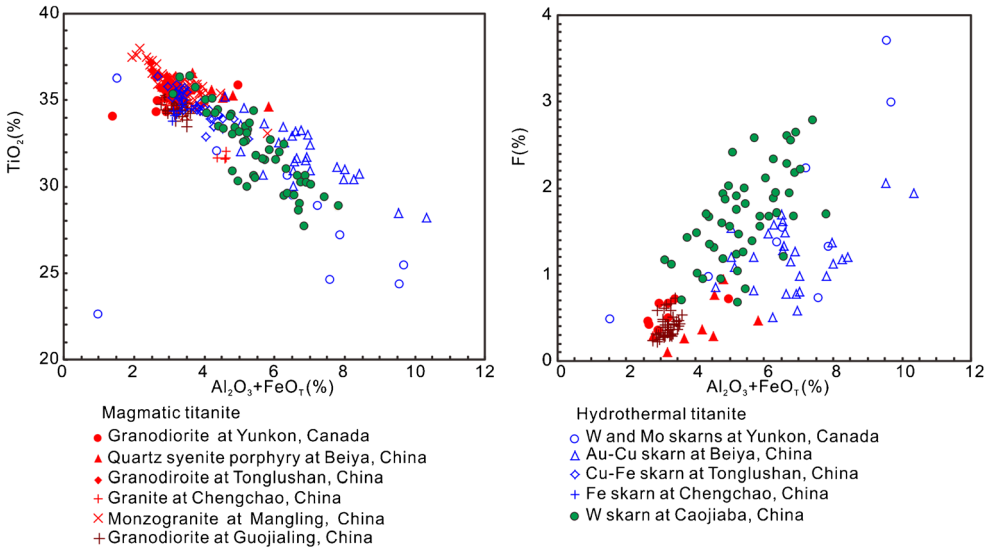

Fig. 9 Binary plots for TiO_2 (**a**) or F (**b**) versus $Al_2O_3 + FeO_T$ in titanites from the Caojiaba tungsten deposit compared with magmatic and hydrothermal titanite (Li et al. 2010;Che et al. 2013; Deng et al. 2015; Fu et al. 2016a; Jiang et al. 2016; Hu et al. 2017b, 2017c)

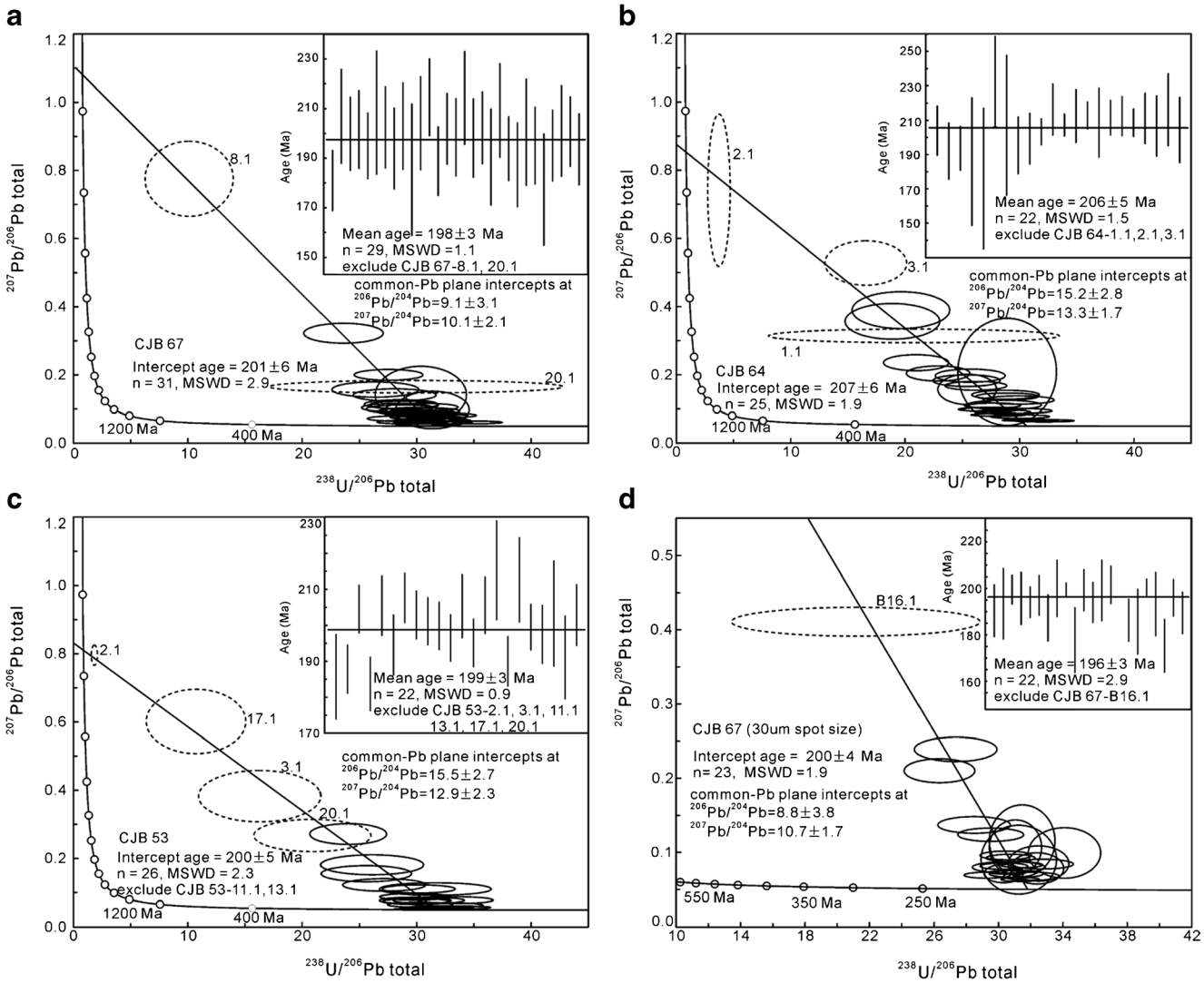

Fig. 10 Tera–Wasserburg diagram and weighted mean plots of age data for titanites from the Caojiaba tungsten deposit

isotope composition is not precisely known, and the initial $^{207}Pb/^{206}Pb$ is calculated as the Y–intercept on the plot. Subsequently, the individual ^{207}Pb–corrected $^{206}Pb/^{238}U$ ages can be calculated for the weighted average age (Fig. 10), which represents the titanite age. Common Pb correction using this method has recently been demonstrated effective in U–Pb dating of hydrothermal titanite from a skarn Au deposit in southwestern China (Fu et al. 2016a).

A total of 31 analyses were obtained on 23 titanite grains from mineralized skarn sample CJB 67. The uncorrected total Pb data define a linear array yielding a lower intercept age of 201 ± 6 Ma (MSWD = 2.9), and most data are nearly concordant plotting nearby in the lower intercept (Fig. 10a). Two spots (CJB 67–8.1 and CJB 67–20.1) yield ^{207}Pb–corrected $^{206}Pb/^{238}U$ ages of 53 ± 37 Ma and 181 ± 32 Ma with large errors (ESM Table 3), and 29 other analyses give a weighted mean ^{207}Pb–corrected $^{206}Pb/^{238}U$ age of 198 ± 3 Ma (2σ, n = 29; MSWD = 1.1; Fig. 10a). A total of 25 analyses were obtained on 24 titanite grains from mineralized skarn sample CJB 64, and the uncorrected total Pb data define a linear array yielding a lower intercept age of 207 ± 6 Ma (MSWD = 1.9; Fig. 10b). Spots CJB 64–1.1, CJB 64–2.1, and CJB 64–3.1 give ^{207}Pb-corrected $^{206}Pb/^{238}U$ ages of 205 ± 51 Ma, 245 ± 191 Ma, and 154 ± 19 Ma with large errors (ESM Table 3), and 22 other analyses give a weighted mean ^{207}Pb-corrected $^{206}Pb/^{238}U$ age of 206 ± 5 Ma (2σ, n = 22; MSWD = 1.5; Fig. 10b). A total of 28 analyses were obtained on 16 titanite grains from mineralized skarn sample CJB 53. Spots CJB 53–11.1 and CJB 53–13.1 have total $^{238}U/^{206}Pb$ and $^{207}Pb/^{206}Pb$ with large errors (ESM Table 3), other uncorrected total Pb data define a linear array yielding a lower intercept age of 200 ± 5 Ma (MSWD = 2.3; Fig. 10c). Spots CJB 53–2.1, CJB 53–3.1, CJB 53–11.1, CJB 53–13.1, CJB 53–17.1, and CJB 53–20.1 give ^{207}Pb–corrected $^{206}Pb/^{238}U$ ages of 301 ± 54 Ma, 228 ± 34 Ma, 570 ± 1578 Ma, 189 ± 168 Ma, 184 ± 41 Ma, and 221 ± 23 Ma with large errors (ESM Table 3), respectively, and 22 other analyses yield a weighted mean ^{207}Pb–corrected $^{206}Pb/^{238}U$ age of 199 ± 3 Ma (2σ, n = 22; MSWD = 0.9; Fig. 10c).

Duplicate analyses of 23 spots of 30 μm were obtained on 19 titanite grains from the mineralized skarn sample CJB 67. The uncorrected total Pb data define a linear array yielding a lower intercept age of 200 ± 4 Ma (MSWD = 1.9), and most data are nearly concordant plotting close to the lower intercept (Fig. 10d). Spot CJB 67–B16.1 yields a ^{207}Pb–corrected $^{206}Pb/^{238}U$ age of 161 ± 25 Ma with a large error (ESM Table 3), and 22 other analyses yield a weighted mean ^{207}Pb–corrected $^{206}Pb/^{238}U$ age of 196 ± 3 Ma (2σ, n = 22; MSWD = 2.9; Fig. 10d).

Discussion

Origin of titanite

Titanite is a widespread accessory mineral in igneous rocks, metamorphic rocks, and hydrothermal mineral deposits such as skarns (Frost et al. 2000). Titanite grains of different origins can be distinguished by their paragenetic mineral assemblages, textures, and chemical compositions (Aleinikoff et al. 2002; Li et al. 2010; Che et al. 2013). The titanite grains in this study coexist with retrograde chlorite and biotite (Fig. 7a, b), indicating a hydrothermal origin, which is supported by the following additional lines of evidence.

Firstly, the titanite grains are irregular in shape and exhibit patchy zoning highlighted on BSE images (Fig. 7d–f). This is similar to other skarn deposits (e.g., Li et al. 2010; Che et al. 2013; Deng et al. 2015; Hu et al. 2017b), and distinct from the oscillatory zoning in magmatic titanite (e.g. Frost et al. 2000; Aleinikoff et al. 2002).

Secondly, titanite consists of chains of corner-sharing Ti octahedra sites and Si tetrahedral sites, which enclose the large seven–fold Ca site. The mineral typically contains large ion elements, including Al, Fe, and F, in its crystal lattice (Frost et al. 2000). As shown in Fig. 9, the titanite grains from Caojiaba share similar compositions as hydrothermal titanite from other skarn deposits (Li et al. 2010; Che et al. 2013; Deng et al. 2015; Fu et al. 2016a). Such titanite crystals are compositionally different from magmatic titanite (Fig. 9). The linear correlations between Al_2O_3 + FeOT and F or TiO_2 (Fig. 9a–b) in this study indicate that Al and Fe substitute for the Ti octahedral site with an additional Al-involving reaction ($(Al, Fe)^{3+} + (F, OH)^{-} \leftrightarrow Ti^{4+} + O^{2-}$), which are common in skarn deposits (Li et al. 2010; Che et al. 2013).

Age of tungsten mineralization

High-grade ores in tungsten skarn deposits are commonly associated with retrograde mineral assemblages, as are abundant titanite and apatite (Einaudi et al. 1981). Conventional chemical and in situ LA–ICPMS dating of titanite grains collected from skarn deposits show that the mineral is a reliable geochronometer (e.g., Romer and Öhlander 1994; Frost et al. 2000; Chiaradia et al. 2009; Li et al. 2010; Deng et al. 2015; Fu et al. 2016a). In this study, in situ SHRIMP U–Pb dating of hydrothermal titanite grains coexisting with scheelite (Fig. 7) in petrographic thin sections provide $^{206}Pb/^{238}U$ ages of 198 ± 3 Ma, 199 ± 3 Ma, and 206 ± 5 Ma for three samples

(Fig. 10a–c). Duplicate analyses of sample CJB 67 with a 30 μm spot size also yield a $^{206}Pb/^{238}U$ age of 196 ± 3 Ma, which is the same within error as the 198 ± 3 Ma age determined using the 15 μm spot size (Fig. 10d).

Genesis of the Caojiaba tungsten deposit

The Caojiaba deposit has several features in common with other well-studied tungsten skarn deposits worldwide. It is characterized by an early prograde (garnet and pyroxene) skarn overprinted by a retrograde skarn, and then both are cut by scheelite-bearing quartz veins (Meinert et al. 2005). The SHRIMP U–Pb ages for the hydrothermal titanite at Caojiaba are much younger than the age of the Devonian host rocks, which does not support sedimentary genetic models for the tungsten mineralization, as has been previously suggested (Qian and Jiang 1983).

Tungsten skarn deposits have been subdivided into reduced and oxidized categories (Einaudi et al. 1981). Evidence supporting a classification of Caojiaba as a distal reduced tungsten skarn includes:

(1) Our new ages show that the Caojiaba tungsten deposit formed between 206 and 196 Ma, and this overlaps with the 228–201 Ma magmatism along the margin of the Shaoyang Basin (Fig. 1b; ESM Table 1). Monazite and zircon U–Pb dating provides age constraints of the earlier regional ductile shearing between 243 and 226 Ma in XZMP (Chu et al. 2012b). Quartz–scheelite-sulfide veins at Caojiaba are not affected by ductile deformation (Fig. 4). This is in contrast to scheelite deposits formed from metamorphic fluids that commonly occur as veins showing evidence of both ductile and brittle deformation in metamorphic host rocks (Cave et al. 2017). Oscillatory zoning of coarse-grained scheelite in the CL image (Fig. 5j) from Caojiaba are similar to those from granite-related deposits, and different from homogenous CL image of scheelite from orogenic Au systems (Poulin et al. 2016).

Scheelite has been reported as an accessory mineral formed during the post-magmatic hydrothermal stage of Triassic granitic rocks with high W content of 21 to 90 ppm in XZMP (HNBGMR 1988; Kong et al. 2014). Bouguer gravity and aeromagnetic anomalies suggest that hidden granitic intrusions may be present beneath the Caojiaba deposit (Qian and Jiang 1983; Rao et al. 1999). The $\delta^{34}S$ values of the pyrrhotite, pyrite, and chalcopyrite coexisting with scheelite at Caojiaba are +0.1 to +0.5 ‰, −0.6 ‰, and − 3.4 to +3.1 ‰, respectively (unpublished data), suggesting to a magmatic source for the sulfur. Therefore, we infer that Caojiaba is a magmatic–hydrothermal tungsten deposit associated with emplacement of late stage of Late Triassic granitic rocks, rather than a deposit related to regional metamorphism or sedimentary processes.

(2) The Caojiaba skarn mineral assemblage is dominated by low andraditic garnet ($Ad_{0.7–21.9}$) and hedenbergitic pyroxene ($Hd_{52.9–77.3}$) (ESM Table 2; Fig. 8). This is similar to the well-studied reduced tungsten skarns at Cantung–Mactung in Canada and Great Dike in Zimbabwe (Einaudi et al. 1981; Zaw and Singoyi 2000), as well as the Darongxi tungsten deposit in XZMP (Fig. 8). The retrograde biotite–chlorite mineral assemblage (Figs. 4f and 5c–e) and the presence of pyrrhotite coexisting with low MoO_3 content (0.01–0.16 wt%) scheelite (ESM Table 2) indicate a reduced W skarn deposit at Caojiaba (Newberry 1998).

Possible relationship between W and Sb–Au deposits

Whether or not a relationship between W–Sn and Sb–Au deposits exists remains controversial. Romer and Kroner (2016, 2018) proposed contrasting factors controlling the distribution of Phanerozoic W–Sn versus Au mineralization, but, at the same time, there is a commonly recognized association of W and Au in quartz veins in many deposits. Scheelite is commonly present in gold deposits hosted by metamorphic rocks (Boyle 1979). Several orogenic gold deposits have the Au–As–Te–W metal association (Goldfarb and Groves 2015). In addition, tungsten is broadly associated with gold in the intrusion-related gold deposits in W–Sn provinces (Thompson et al. 1999). Lang and Baker (2001) proposed a model to illustrate proximal W–(Au–Cu) skarns and distal Au–Sb veins surrounding causative plutons in intrusion-related gold systems.

Our study shows that Caojiaba is a 206–196 Ma distal reduced tungsten skarn deposit with Au (up to 1.5 ppm) and Sb (up to 0.33 wt%) contents (Fig. 2a). Coarse-grained scheelite (Figs. 4j and 5l) coexisting with stibnite from the Xiejiashan Sb–Au (W) deposit (Fig. 1b) yields a Sm–Nd isochron age of 210 ± 2 Ma (Zhang et al. 2018). The Re–Os age of 195 ± 36 Ma for pyrite coexisting with native gold in the Longshan W-bearing Sb–Au deposit

(Fig. 1b) overlaps with the ages of nearby felsic dykes, indicating magmatism may have played a vital role in the formation of the deposit (Fu et al. 2016b). These above ages and consistent W–Sb–Au metal association indicate a possible link between W and Sb–Au mineralization in XZMP.

Previous studies proposed a genetic relationship between low-temperature Sb–Au deposits in XZMP and granite-related W–Sn mineralization to the east in the Cathaysia Block (Hu and Zhou 2012; Mao et al. 2013; Hu et al. 2017a). In addition to the 206–196 Ma distal reduced skarn tungsten deposit at Caojiaba, granite-related Late Triassic tungsten deposits have also been discovered and recognized at Darongxi, Muguanyuan, Shaxi, Zhongcun, and Niujiaojie (Fig. 1b) in XZMP. For example, the Darongxi deposit (Fig. 1b) is a proximal reduced skarn tungsten deposit containing a resource of 40,000 t WO_3 grading 0.49 wt%, where the mineralization is hosted by Neoproterozoic sandstone, marble, and shale located less than 500 m from granite contacts (Zhang 2013; Zhang et al. 2014). A molybdenite Re–Os weighted mean age of 219 ± 1 Ma is slightly younger than the zircon U–Pb age of 224 ± 1 Ma for the nearby granite at Dashengshan (Fig. 1b; Zhang et al. 2014). The Muguanyuan deposit (Fig. 1b), with a resource of 25,300 t WO_3 grading 0.12 wt% and averaging 2.8 ppm Au, forms disseminated and veinlet-hosted ores hosted by the Sanxianba granite porphyry stock (0.1 km^2) (Tang et al. 2016; Luo and Shu 2017). Molybdenite from this deposit yields a weighted mean Re–Os age of 226 ± 5 Ma overlap the intrusion age of 222 ± 2 Ma (unpublished data). Quartz vein-hosted W deposits exceeding 100,000 t WO_3 are hosted by 223–214 Ma granitic intrusions at Chongyangping and Wawutang (Fig. 1b) (Su et al. 2016). These above results demonstrate that 226–196 Ma granite-related W mineralization in XZMP overlap with the broad period of the 230–200 Ma (Hu and Zhou 2012) granite-related W–Sn deposits in the Cathaysia Block, and 210–200 Ma low-temperature Sb–Au deposits hosted by Proterozoic metamorphosed rocks in XZMP (Hu et al. 2017a). These Sb–Au deposits commonly contain scheelite with elevated W contents up to 0.47 wt% WO_3 (Peng and Frei 2004; Zhu and Peng 2015). Felsic dykes are spatially associated with 27 Sb–Au deposits in the region, such as at the Fuzhuxi and Liaojiaping Sb–Au, Banxi Sb, and Chanziping Au deposits (Fig. 1b; Liu 1996). Mineralized granite and granite porphyry have K–Ar age of 204 Ma to 194 Ma (Peng and Frei 2004; Hu et al. 2017a). Stable isotope data (H–O–S–C) indicate that Sb–Au deposits in XZMP may have formed from magmatic fluids, which leached the ore-forming elements from the metamorphic basement rocks (Hu et al. 2017a). These above features indicate a possible link between W and Sb–Au mineralization in XZMP.

Conclusions

The mineral paragenesis at Caojiaba is similar to reduced tungsten skarns worldwide, and contains low andraditic garnet ($Ad_{0.7–21.9}$) and hedenbergitic pyroxene ($Hd_{52.9–77.3}$) skarn assemblages. The deposit formed at 206 to 196 Ma indicated by the SHRIMP U–Pb ages for hydrothermal titanite coexisting with scheelite. The ages overlap with the 228–201 Ma magmatism in XZMP. The combined mineralogical and geochronological constraints indicate that Caojiaba is a distal reduced W skarn deposit. The 226–196 Ma granite-related W mineralization recognized throughout XZMP has a possible link with the widespread Sb–Au mineralization in the region.

Acknowledgments This work was supported by the National Basic Research Program of China (2014CB440902) and the National Science Foundation of China (41573042, 41430314 and 41372090). We thank the No. 407 Geological Team of the Bureau of Geology and Mineral Exploration and Development of Hunan Province. We also thank Dr. Zhu Qiaoqiao, Li Wei, Chen Zhenyu, Chen Lei, and Chen Xiaodan for their assistance during fieldwork and analyses. Associate Editor Rolf Romer, Editor Georges Beaudoin, Richard Tosdal, and an anonymous reviewer are thanked for constructive reviews that greatly improved the quality of this paper. We truly appreciate the constructive comments and detailed editing by Richard Goldfarb.

References

Aleinikoff JN, Wintsch R, Fanning CM, Dorais M (2002) U–Pb geochronology of zircon and polygenetic titanite from the Glastonbury Complex, Connecticut, USA: an integrated SEM, EMPA, TIMS, and SHRIMP study. Chem Geol 188: 125–147

Aleinikoff JN, Wintsch R, Tollo RP, Unruh DM, Fanning CM, Schmitz MD (2007) Ages and origins of rocks of the Killingworth dome, south–central Connecticut: implications for the tectonic evolution of southern New England. Am J Sci 307:63–118

Boyle RW (1979) The geochemistry of gold and its deposits. Geol Surv Can Bull 280:1–584

Cave BJ, K. Pitcairn I, Craw D, Large RR, Thompson JM, Johnson S C (2017) A metamorphic mineral source for tungsten in the turbidite-hosted orogenic gold deposits of the Otago Schist, New Zealand Mineralium Deposita 52: 515–537

Che XD, Linnen RL, Wang RC, Groat LA, Brand AA (2013) Distribution of trace and rare earth elements in titanite from

tungsten and molybdenum deposits in Yukon and British Columbia, Canada. Can Mineral 51:415–438

Chiaradia M, Vallance J, Fontboté L, Stein H, Schaltegger U, Coder J, Richards J, Villeneuve M, Gendall I (2009) U–Pb, Re–Os, and $^{40}Ar/^{39}Ar$ geochronology of the Nambija Au–skarn and Pangui porphyry Cu deposits, Ecuador: implications for the Jurassic metallogenic belt of the Northern Andes. Mineral Deposita 44: 371–387

Chu Y, Lin W, Faure M, Wang QC, Ji WB (2012a) Phanerozoic tectonothermal events of the Xuefengshan Belt, central South China: implications from U–Pb age and Lu–Hf determinations of granites. Lithos 150:243–255

Chu Y, Faure M, Lin W, Wang Q, Ji WB (2012b) Tectonics of the Middle Triassic intracontinental Xuefengshan Belt, South China: new insights from structural and chronological constraints on the basal décollement zone. Int J Earth Sci 101:2125–2150

Deng XD, Li JW, Zhou MF, Zhao XF, Yan DR (2015) In–situ LA–ICPMS trace elements and U–Pb analysis of titanite from the Mesozoic Ruanjiawan W–Cu–Mo skarn deposit, Daye district, China. Ore Geology Rev 65:990–1004

Einaudi MT, Meinert LD, Newberry RJ (1981) Skarn deposits. Economic Geology 75th Anniversary Volume: 317–391

Frost B, Chamberlain K, Schumacher J (2000) Sphene (titanite): phase relations and role as a geochronometer. Chem Geol 172:131–148

Fu SL, Hu RZ, Bi XW, Chen YW, Yang JH, Huang Y (2015) Origin of Triassic granites in central Hunan Province, South China: constraints from zircon U–Pb ages and Hf and O isotopes. Int Geol Rev 57:97–111

Fu Y, Sun X, Zhou H, Lin H, Yang T (2016a) In-situ LA–ICP–MS U–Pb geochronology and trace elements analysis of polygenetic titanite from the giant Beiya gold–polymetallic deposit in Yunnan Province, Southwest China. Ore Geol Rev 77:43–56

Fu SL, Hu RZ, Chen YW, Luo JC (2016b) Chronology of the Longshan Au–Sb deposit in central Hunan Province: constraints from pyrite Re–Os and zircon U–Th/He isotopic dating. Acta Petrol Sin 32:3507–3517 (in Chinese with English abstract)

Goldfarb RJ, Groves DI (2015) Orogenic gold common or evolving fluid and metal sources through time. Lithos 233:2–26

HNBGMR (Bureau of Geology and Mineral Resources of Hunan Province) (1988) Regional geology of the Hunan Province. Geological Publishing House, Beijing (in Chinese with English abstract)

HNBGMR (Bureau of Geology and Mineral Resources of Hunan Province) (2015) Geology of tungsten deposit in Tanxi mining area, Xinshao County, Hunan Province. China. Unpublished research Report (in Chinese)

Hu RZ, Fu SL, Huang Y, Xiao JF (2017a) The giant South China Mesozoic low–temperature metallogenic domain: reviews and a new geodynamic model. J Asian Earth Sci 137:9–34

Hu H, Li JW, McFarlane CRM (2017b) Hydrothermal titanite from the Chengchao iron skarn deposit: temporal constraints on iron mineralization, and its potential as a reference material for titanite U–Pb dating. Mineral Petrol 111:593–608

Hu H, Li JW, McFarlane CRM, Luo Y, McCarron T (2017c) Textures, trace element compositions, and U–Pb ages of titanite from the mangling granitoid pluton, east Qinling Orogen: implications for magma mixing and destruction of the North China Craton. Lithos 284–285:50–68

Hu RZ, Zhou MF (2012) Multiple Mesozoic mineralization events in South China—an introduction to the thematic issue. Mineral Deposita 47:579–588

Jiang P, Yang KF, Fan HR, Liu X, Cai YC, Yang YH (2016) Titanite-scale insights into multistage magma mixing in early cretaceous of NW Jiaodong terrane, North China Craton. Lithos 258–259: 197–214

Kong LB, Lyu SJ, Li YD (2014) Geological characteristics and ore-searching prospect of the Shaxi tungsten deposit in Chongyangping, Hunan Province. Geol Miner Resour South China 30:375–382 (in Chinese with English abstract)

Kwak TAP (1987) W–Sn skarn deposits and related metamorphic skarns and granitoids. Dev Econ Geol 24:1–450

Lang JR, Baker T (2001) Intrusion–related gold systems: the present level of understanding. Mineral Deposita 36:477–489

Li JW, Deng XD, Zhou MF, Liu YS, Zhao XF, Guo JL (2010) Laser ablation ICP–MS titanite U–Th–Pb dating of hydrothermal ore deposits: a case study of the Tonglushan Cu–Fe–Au skarn deposit, SE Hubei Province, China. Chem Geol 270:56–67

Liu JS (1996) Relationship between felsic dikes and antimony–gold mineralization in central Hunan Province. Geol Explor Non–Ferrous Met 5:321–326 (in Chinese with English abstract)

Ludwig K (2012) User's manual for Isoplot version 3.75–4.15: a geochronological toolkit for Microsoft. Excel Berkley Geochronological Center Special Publication, 5

Luo SC, Shu CL (2017) The geological features and relationship of the Muguayuan tungsten-gold deposit in Taojiang, Hunan. Mine Eng Constr 2017(2):98–99 (in Chinese with English abstract)

Mao JW, Cheng YB, Chen MH, Pirajno F (2013) Major types and time–space distribution of Mesozoic ore deposits in South China and their geodynamic settings. Mineral Deposita 48:267–294

Meinert LD, Dipple GM, Nicolescu S (2005) World skarn deposits. Economic Geology 100th Anniversary: 299–336

Newberry RJ (1998) W- and Sn-skarn deposits: a 1998 status report. Mineralogical Association of Canada short course series 26: 289–335

Peng B, Frei R (2004) Nd–Sr–Pb isotopic constraints on metal and fluid sources in W–Sb–Au mineralization at Woxi and Liaojiaping (Western Hunan, China). Mineral Deposita 39: 313–327

Poulin RS, McDonald AM, Kontak DJ, McClenaghan MB (2016) On the relationship between cathodoluminescence and the chemical composition of scheelite from geologically diverse ore-deposit environments. Can Mineral 54:1147–1173

Qian YQ, Jiang SG (1983) The discovery and geological characteristics of the Caojiaba stratabound scheelite skarn deposit at Xinshao, Hunan. Hunan Geol 2:26–35 (in Chinese)

Raith JG, Stein HJ (2000) Re–Os dating and sulfur isotope composition of molybdenite from tungsten deposits in western Namaqualand, South Africa: implications for ore genesis and the timing of metamorphism. Mineral Deposita 35:741–753

Rao JR, Luo JL, Yi ZJ (1999) The mantle–crustal tectonic metallogenic model and ore–prospecting prognosis in the Xikuangshan antimony ore field. Geophys Geochem Explor 23:241–249 (in Chinese with English abstract)

Romer RL, Kroner U (2016) Phanerozoic tin and tungsten mineralization—tectonic controls on the distribution of enriched protoliths and heat sources for crustal melting. Gondwana Res 31:60–95

Romer RL, Kroner U (2018) Paleozoic gold in the Appalachians and Variscides. Ore Geol Rev 92:475–505

Romer RL, Öhlander B (1994) U–Pb age of the Yxsjöberg tungsten–skarn deposit, Sweden. GFF 116:161–166

Stacey JS, Kramers JD (1975) Approximation of terrestrial lead isotope evolution by a two–stage model. Earth Planet Sci Lett 26: 207–221

Su KM, Lv SJ, Kong LB, Yang FQ, Xiang JF (2016) Geological characteristics, metallogenetic regularity and model of quartz vein type tungsten deposits in Chongyangping, Hunan Province. Mineral Deposits 35:902–912 (in Chinese with English abstract)

Tang SL, Yan DP, Qiu L, Gao JF, Wang CL (2014) Partitioning of the cretaceous Pan–Yangtze Basin in the central South China block by exhumation of the Xuefeng Mountains during a transition from extensional to compressional tectonics. Gondwana Res 25:1644–1659

Tang YM, Zhao QH, Luo SC (2016) Geological charactertics and metallogenetic regularity of the Muguayuan porphyry tungsten deposit in Taojiang, Hunan. Western Resouces (3): 94–95 (in Chinese)

Thompson JFH, Sillitoe RH, Baker T, Lang JR, Mortensen JK (1999) Intrusion–related gold deposits associated with tungsten–tin provinces. Mineral Deposita 34:323–334

Xie GQ, Mao JW, Li WFB, Zhang ZY (2018) Granite–related Yangjiashan tungsten deposit, southern China. Mineral Deposita. https://doi.org/10.1007/s00126-018-0805-5

Zaw K, Singoyi B (2000) Formation of magnetite–scheelite skarn mineralization at Kara, northwestern Tasmania: evidence from mineral chemistry and stable isotopes. Econ Geol 95:1215–1230

Zhang LS (2013) Skarn and ore genesis of the Darongxi tungsten deposit, western Hunan. Dissertation, Central South University (in Chinese with English abstract)

Zhang LS, Peng JT, Hu AX, Lin FM, Zhang T (2014) Re–Os dating of molybdenite from Darongxi tungsten deposit in western Hunan and its geological implications. Mineral Deposits 33:181–189 (in Chinese with English abstract)

Zhang ZY, Xie GQ, Mao JW, Liu WG, Zhu QQ, Li W (2018) Sm–Nd dating and trace element geochemistry of scheelite for the Xiejiashan Sb–Au–W deposit in the Xiangzhong metallogenic province, southern China. In preparation

Zhang ZY, Xie GQ, Zhu QQ, Li W, Han YX, Wang FL (2016) Mineralogical characteristics of skarns in the Caojiaba large tungsten deposit of central Hunan Province and their geological significance. Mineral Deposits 35:335–348 (in Chinese with English abstract)

Zhao WW, Zhou MF, Li YHM, Zhao Z, Gao JF (2017) Genetic types, mineralization styles, and geodynamic settings of Mesozoic tungsten deposits in South China. J Asian Earth Sci 137:109–140

Zhu YN, Peng JT (2015) Infrared microthermometric and noble gas isotope study of fluid inclusions in ore minerals at the Woxi orogenic Au–Sb–W deposit, western Hunan, South China. Ore Geol Rev 65: 55–69